Energy & Environmental Science

ROYAL SOCIETY OF CHEMISTRY

PAPER

View Article Online
View Journal

Cite this: DOI: 10.1039/d6ee02250b

Nonplanar tertiary-N extended nitrobenzene enables insoluble and low-energy-barrier organic small-molecule cathodes for high-performance aqueous batteries

Ziyang Song, [abc] Qi Huang, [d] Yaokang Lv, [e] Lihua Gan [ac] and Mingxian Liu *[ac]

Organic small molecules with a high mass content ratio of redox-active sites are promising high-capacity cathode materials for aqueous zinc batteries, but their strong interaction with aqueous electrolytes causes serious dissolution and limited cycling life. Here, we demonstrate nonplanar tertiary-N extended nitrobenzene, which harnesses its strong intramolecular π–π interaction beyond the H_2O dissociation energy, to create an insoluble and low-energy-barrier nitroarene (TNB) small-molecule cathode. Two rotating *tert*-N linkages bring the extended π-aromatic nonplanar configuration of TNB, exhibiting a maximum negative intramolecular potential energy of −35.8 kcal mol^{-1} compared to its large repulsive force of 15.1 kcal mol^{-1} in H_2O medium. Consequently, the intramolecular π–π interactions within TNB are significantly stronger than its interactions with H_2O molecules, thereby suppressing dissolution in the aqueous electrolyte and extending the battery lifespan to the state-of-the-art level (180 000 cycles). Meanwhile, the nonplanar structure of TNB allows for 98.9% utilization of nitro/*tert*-N motifs with low activation energy (0.23 eV), liberating superior capacity (430 mAh g^{-1}) and large-current tolerance (100 A g^{-1}). Significantly, this nonplanar molecular design shows promising preliminary generalizability to develop versatile insoluble carboxylic, cyano, and imine compounds. These proof-of-concept results suggest a potential paradigm for highly active and ultrastable organic molecules towards better aqueous batteries.

Received 8th April 2026,
Accepted 1st June 2026

DOI: 10.1039/d6ee02250b

rsc.li/ees

Broader context

Aqueous zinc batteries are emerging as prevalent energy storage systems due to resource richness, operational safety, and the high capacity of Zn anodes. Benefiting from sustainability and broad structural and functional tunability, aromatic organic materials stand out as promising cathodes for propelling zinc–organic batteries (ZOBs). Organic small molecules with high-density active sites that allow greater electron transfer have attracted broad interest as high-capacity cathodes for ZOBs. However, they suffer from high solubility in aqueous electrolytes due to the strong interaction between their polar redox-active motifs and aqueous solvents of electrolytes, triggering irreversible capacity loss after cycling. In this work, we describe nonplanar tertiary-N extended nitrobenzene with stronger intramolecular π–π interactions (−35.8 kcal mol^{-1}) than the dissociation energy of H_2O (15.1 kcal mol^{-1}) in aqueous electrolytes. This enables the insoluble and low-energy-barrier *N*,*N*,*N*′,*N*′-tetrakis(4-nitrophenyl)-1,4-benzenediamine small molecule cathode, which liberates excellent structural anti-dissolution in aqueous electrolytes to afford a state-of-the-art cycling lifespan (180 000 cycles) for ZOBs. Notably, this nonplanar molecular structure can be further generalized to develop a family of carboxylic, cyano, and imine compounds. This work marks significant progress in discovering insoluble and low-energy-barrier redox-active organic small molecules, which will inspire further efforts to enrich the organic nonplanar structure library in the energy field.

[a] *School of Chemical Science and Engineering, State Key Laboratory of Cardiovascular Diseases and Medical Innovation Center, Shanghai East Hospital, Tongji University, 1239 Siping Road, Shanghai 200092, China. E-mail: liumx@tongji.edu.cn*
[b] *State Key Laboratory of Water Pollution Control and Green Resource Recycling, College of Environmental Science and Engineering, Advanced Research Institute, Tongji University, 1239 Siping Road, Shanghai 200092, China*
[c] *Shanghai Key Lab of Chemical Assessment and Sustainability, Shanghai 200092, China*
[d] *State Key Laboratory of Photovoltaic Science and Technology, Institute of Optoelectronics, College of Future Information Technology, Fudan University, Shanghai 200438, China*
[e] *College of Chemical Engineering, Zhejiang University of Technology, 18 Chaowang Road, Hangzhou 310014, China*

Introduction

With growing requirements for sustainable and efficient energy storage solutions, rechargeable aqueous batteries have inspired great attention because of their high energy supply, operational safety, and natural abundance.[1–5] Currently, aqueous Zn-ion batteries prevail as the leading system, and are highly praised for the low potential (−0.76 V *vs.* standard hydrogen electrode), high capacity (820 mAh g^{-1}), and environmental friendliness of the Zn anodes.[6–10] One significant task for the development of Zn batteries is seeking suitable cathode materials.[11–15] Unlike resource-limited mineral-derived inorganic materials, aromatic organic materials (*e.g.*, quinones, azines, azobenzenes, nitroaromatics) possess resources sustainability, and customizable functions,[16–21] making them promising cathode candidates for Zn–organic batteries (ZOBs). Featured with high-density redox-active sites, π-aromatic organic small molecules allow more electron transfer and have captured significant attention as high-capacity cathodes for ZOBs.[22–25] Unfortunately, they are easily dissolved in aqueous electrolytes due to their strong interactions with aqueous solvents, leading to fast capacity loss after cycling.[26–28]

To alleviate the dissolution concern and improve cycling stability of organic small molecules, a prevailing strategy has been implemented, *i.e.*, polymerizing soluble molecules into covalent organic frameworks (COFs) or π-conjugated polymers.[29–33] The first example affords planar π-conjugated skeleton robustness to decrease the solubility in aqueous electrolytes for long-life ZOBs (20 000 cycles).[34] However, this inevitably adds a high proportion of redox-inactive benzene ring nodes to the organic skeleton and/or faces synthesis/purification complexity.[34–36] Another promising approach is the use of polymers, whose robust solid structure can suppress dissolution and prolong battery lifespan (10 000 cycles).[37–39] Unfortunately, twisted polymeric chains and random folding structures often bring high spatial reaction energy barriers for built-in redox-active units, limiting the utilization of multi-redox motifs with reduced available capacities (<250 mAh g^{-1}).[32,33,40,41] Overall, π-conjugated COFs or polymers face a tricky trade-off between high capacity and long life, leaving a large space for structural engineering to strategically reform ZOBs.

To bridge these gaps, exploring insoluble organic small molecules with robust structures and low-energy-barrier functions without compromising their multi-redox capabilities stands as a pivotal objective in pursuing better ZOBs. So far, there are three prevailing solutions to conquer the dissolution issue of organic small molecules for ZOBs: constructing stable intramolecular H-bonds with inert amine donators,[17,42] carbon encapsulation,[13,43] and planar structure extension with benzene rings.[26,44,45] These methods broaden the electrochemical horizons of anti-dissolution organic small molecules, affording long-lasting ZOBs (up to 50 000 cycles). Unfortunately, they often need to integrate a high proportion of inactive constituents with high energy barriers, limiting their redox capacity (<300 mAh g^{-1}) and/or rate performance (<20 A g^{-1}). π–π stacking interactions are prevalent in aromatic organic molecules owing to the π-electron clouds of benzene rings and play an important role in governing their molecular conformations, properties and performances.[46–49] In essence, the insolubility of aromatic molecules implies that their intramolecular π–π interactions should be stronger than solvation forces generated by water molecules in aqueous electrolytes. Following this principle, we envision creating nonplanar molecular conformations with extended aromatics into water-insensitive insoluble organic skeletons, which not only form strong intramolecular π–π stacking interactions to maintain structural regularity in aqueous electrolytes, but also fully expose redox sites with low spatial energy barriers for multielectron transfer. Consequently, the dissolution concern of organic small molecules should be well solved, thereby propelling ZOBs with dual-high activity and durability, but this has not yet been achieved.

In this work, we report nonplanar tertiary-N extended nitrobenzene with stronger intramolecular π–π interaction than the dissociation energy of H_2O in aqueous electrolytes, which enables insoluble and low-energy-barrier *N*,*N*,*N*′,*N*′-tetrakis(4-nitrophenyl)-1,4-benzenediamine (TNB) small-molecule cathodes for state-of-the-art aqueous ZOBs. Two rotating *tert*-N linkages bring the extended π-aromatic nonplanar configuration of TNB, which shows stronger intramolecular π–π interactions (−35.8 kcal mol^{-1}) than H_2O dissociation forces (15.1 kcal mol^{-1}), thus liberating structural insolubility in aqueous electrolytes to afford a state-of-the-art cycling lifespan (180 000 cycles) for ZOBs. Multi-redox TNB with a nonplanar structure allows 98.9% utilization of n–p fused nitro/*tert*-N motifs with a low energy barrier (0.23 eV) *via* co-storing Zn^{2+} and SO_4^{2-} ions, thereby delivering an ultrahigh capacity and high-rate capability. More importantly, this nonplanar molecular design exhibits encouraging initial generalizability, as further demonstrated by its successful application to carboxylic, cyano, and imine compounds. While additional structural optimization and systematic validation are ongoing, these proof-of-concept results mark significant progress in discovering insoluble and low-energy-barrier redox-active organic small molecules, which will inspire further efforts to enrich the organic nonplanar structure library in the energy field.

Results and discussion

Fig. 1a demonstrates the nonplanar molecular engineering of TNB, which integrates dual-electron-acceptor nitro sites of planar 1,4-dinitrobenzene (DB) and single-electron-donating rotated *tert*-N species of nonplanar triphenylamine (TA) into an extended π-conjugated multi-redox aromatic skeleton (Fig. S1). Generally, due to the two-electron redox capability of each nitro motif,[50] DB delivers high redox activity to trigger multielectron charge storage. However, its small planar structure faces severe dissolution and high reaction energy barriers in aqueous electrolytes, making it difficult for ionic carriers to utilize its buried electroactive nitro groups.[20] In contrast, the rotated p-type *tert*-N site generates a nonplanar structure,[51] which is expected to fully expose low-energy-barrier active sites and achieve structural insolubility of TA. Unfortunately, it is

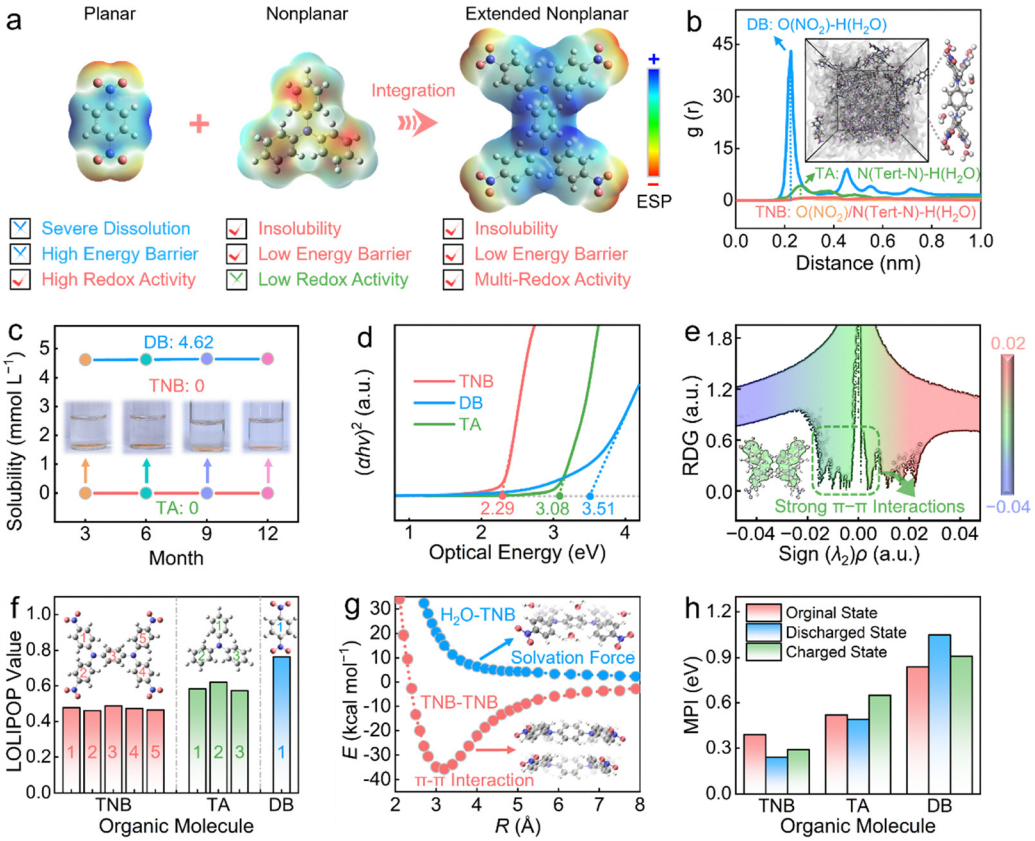

Fig. 1 Structural analysis of organic small molecules. (a) Molecular structures, ESP maps and electrochemical properties of DB, TA and TNB (grey, blue, red, and white balls represent C, N, O, and H atoms, respectively). (b) RDFs of DB, TA and TNB to H_2O (inset: molecular dynamics simulation snapshots of TNB in 3 M $ZnSO_4/H_2O$ solution and corresponding interaction structure between stacked TNB and H_2O). (c) Solubility and photos of $ZnSO_4/H_2O$ solution soaked with DB, TA and TNB for different times. (d) Optical energy gaps of small molecules. (e) RDG scattered points against sign(λ_2)ρ (inset: Gradient isosurface). (f) LOLIPOP values. (g) Calculated potential energy profiles comparing $\pi-\pi$ stacked TNB aggregates *versus* TNB–H_2O solvated structures, revealing energetic preference for intermolecular stacking. (h) Molecular polarity index at different electrochemical states.

trapped by low capacity due to single-electron reactions. Thus, TNB was developed *via* the nonplanar molecular engineering to leverage the merits of DB (high redox activity) and TA (low energy barrier and insolubility), while compensating for their respective flaws (Fig. 1a).

Nuclear magnetic resonance pattern, Fourier transform infrared (FT-IR) spectra, scanning electron microscopy (SEM) images, and X-ray diffraction (XRD) patterns confirm the structural and functional constituents of TNB (Fig. S1–S5). Molecular electrostatic potential (ESP) simulation,[52,53] was applied to infer the electron structures and redox properties of three organic molecules (Fig. S6a–c and Fig. 1a). On the van der Waals surface of DB, two nitro sites show a more negative ESP value of -24.83 kcal mol^{-1} than the *tert*-N motif of TA (-7.82 kcal mol^{-1}), which implies the higher redox activity of DB. In contrast, TNB shows the most negative ESP value of -41.87 kcal mol^{-1}, which makes its redox sites more accessible to electrons and ions. Specifically, four electronegative nitro regions and electropositive *tert*-N sites of TNB are considered as n-type and p-type motifs for the chelation of cationic and anionic carriers, respectively. It highlights the ambipolar redox attribute of TNB, which delivers the ability to store opposite charges.

To decipher the solubility of three organic molecules in a 3 M $ZnSO_4/H_2O$ electrolyte, molecular dynamics (MD) simulations were conducted.[54,55] The radial distribution functions (RDFs) of DB appear to have a significant peak of O(NO_2)–H(H_2O) at the position range of 0.20–0.30 nm (Fig. 1b), which indicates strong H-bonding interactions between highly redox-active nitro functional groups and water molecules, making it easily soluble in the electrolyte. In contrast, RDFs of TA show an insignificant peak of N(C–N)–H(H_2O) at the position of 0.23 nm, implying its negligible interaction with H_2O molecules due to the low redox activity of the *tert*-N motif, thus affording structural stability. Of note, there is no response signal in RDFs for TNB, which indicates that it does not interact with H_2O molecules (illustration of Fig. 1b), supporting structural anti-dissolution.

The dissolution behavior of DB, TA and TNB molecules in a 3 M $ZnSO_4/H_2O$ electrolyte after 3–12 months is further studied by ultraviolet-visible (UV-vis) spectrum analysis. Compared with highly soluble DB (4.62 mmol L^{-1}), the concentration of TNB was assessed to be 0 mmol L^{-1} (Fig. 1c and Fig. S6d–f), which suggests its structural insolubility in aqueous solutions (also reflected by colorless electrolytes, inset of Fig. 1c). Such an

excellent anti-dissolution of TNB is attributed to the extended nonplanar π–π stacking configuration, which spreads excess charges throughout the skeleton and suppresses the TNB–H_2O interaction force to liberate structural robustness, which would promote its stable cycling in aqueous zinc batteries.

The optical energy gap (E_g) from solid-state UV/vis spectra was measured to be 2.29 eV for TNB (Fig. 1d), which is lower than DB (3.51 eV) and TA (3.08 eV), attributed to efficient electron conduction and a high-kinetics redox reaction with low energy barriers. The localized orbital locator-π (LOL-π) color-filled map[55] was further obtained to unravel the electron structure of TNB (Fig. S7). The extended highly π-conjugated nonplanar aromatic structure endows TNB with higher conductivity than those of DB and TA (Fig. S8), which is beneficial for promoting efficient electron delocalization through the whole skeleton and ensuring structural integrity to suppress dissolution in electrolytes (Fig. S9). It is well-known that the extended π–π stacking conjugated structure of organic materials helps to reduce the band gap (ΔE) of the highest occupied molecular orbital (HOMO) and the lowest unoccupied molecular orbital (LUMO).[56–58] Consequently, TNB with an expanded π-conjugated nonplanar structure delivers the lowest ΔE of 3.09 eV (Fig. S10) in comparison to DB (4.78 eV) and TA (4.23 eV), promising convenient electron injection/removal (Fig. S11).

Reduced density gradient (RDG) analysis[59,60] was performed to reveal the intramolecular forces in TNB (Fig. 1e). The strong green spike signals appeared at −0.02–0.02 a.u. of the sign(λ_2)ρ denote powerful intramolecular π–π interactions derived from the large π-conjugation nonplanar structure (also reflected in the corresponding gradient isosurface map, inset of Fig. 1e). In addition, the π-electron localized orbital locator (LOL-π) integrated π over plane (LOLIPOP) method,[56] as a representative of the strength of π–π stacking interactions, was applied to evaluate the π-stacking ability of the TNB molecule (Fig. 1f). Theoretically, the smaller the LOLIPOP value of aromatic rings, the stronger the π–π stacking interactions. Compared to DB (0.765) and TA (0.584–0.621), different aromatic rings of TNB show the smallest LOLIPOP values (0.461–0.488), indicating its strongest π–π stacking intramolecular interactions, which contribute to excellent structural integrity.

Potential energy curves unravel that the intramolecular π–π interaction strength of TNB between adjacent nonplanar structures (TNB–TNB) is significantly stronger than the solvation interaction between H_2O molecules and TNB (TNB–H_2O) (Fig. 1g). Particularly, the strong intramolecular π–π forces can be reflected by the most negative potential energy (E) of −35.8 kcal mol^{-1} at the stacked layer distance (R) of 0.32 nm, in comparison to the large repulsive force of 15.1 kcal mol^{-1} for TNB–H_2O. These results agree with the XRD result (Fig. S5a), whose diffraction peak at 27.3° and a d-spacing of 0.32 nm (Fig. S5b) are attributed to typical π–π stacking of nonplanar structures. Thus, the intramolecular π–π interaction is stronger than the solvation force of H_2O, contributing to the structural insolubility of TNB.

Furthermore, the molecular polarity index (MPI) of DB, TA and TNB molecules was simulated to analyze their solubility during the (dis)charge process (Fig. 1h). The MPI is an indicator for measuring the polarity of organic systems through the features of ESP maps (Fig. 1a). In theory, the larger the MPI, the greater the overall polarity of the molecule and its solubility in H_2O medium.[61] The DB molecule at different electrochemical states shows the largest MPI (0.84–1.05) due to the high partial charge and redox activity of nitro sites. TA exhibits reduced MPI (0.49–0.65) derived from the low reactivity of *tert*-N sites. In contrast, the (dis)charge products of the TNB molecule exhibit the smallest MPI (0.24–0.39) because of the stronger nonplanar π-conjugation effect, and thus the smallest solubility in the H_2O medium, which agrees with the experimental results. Overall, TNB fuses structural insolubility and exposed multi-redox sites with low energy barriers, which are expected to be highly desirable features for activating high-performance ZOBs.

The electrochemical properties of the TNB cathode were investigated in ZOBs by using a Zn metal anode and 3 M $ZnSO_4$/H_2O electrolyte (Fig. S12 and S13). The Zn||TNB battery delivers an ultrahigh specific capacity of 430 mAh g^{-1} at 0.2 A g^{-1} based on galvanostatic (dis)charge (GCD) profiles (Fig. 2a). It exceeds Zn||DB (92 mAh g^{-1}) and Zn||TA (109 mAh g^{-1}) cells, implying its excellent charge storage capability. Cyclic voltammogram (CV) profiles of the Zn||TNB cell at various scan rates of 1–10 mV s^{-1} show three pairs of redox peaks (marked as P_{R1}, P_{R2}, P_{R3}, P_{O1} P_{O2}, and P_{O3}, Fig. 2b), unveiling the electrochemical reversibility and triple-redox behavior of the TNB cathode with an average discharge voltage of 0.9 V. Furthermore, compared with Zn||DB and Zn||TA cells, the Zn||TNB battery achieves highly reversible capacities and excellent rate metrics at 0.2–100 A g^{-1} (Fig. 2c and Fig. S14 and Table S1), highlighting the multi-redox nonplanar structure advantage of TNB. Impressively, a high-capacity–voltage TNB cathode endows the Zn||TNB battery with a desirable energy output of 385 Wh kg$^{-1}_{TNB}$ (Fig. S15a and b), which holds potential to compete with recently reported organic materials used for aqueous batteries (Fig. 2d and Table S2).[7,11,22,38,62–67]

The Zn||TNB battery displays stable capacities after 10 000 cycles at 1 A g^{-1} (Fig. S16), reflecting the desirable electrochemical reaction process and the intrinsic structural stability of the TNB cathode. It also shows superb stability with 84.1% capacity retention over 180 000 cycles at 10 A g^{-1} (Fig. 2e and Fig. S16b), surpassing the batteries assembled by DB (15.4%) and TA (76.8%) cathodes. By leveraging the synergistic advantages of planar DB (high activity) and nonplanar TA (low energy barrier and insolubility) while compensating for their respective shortcomings, two rotating *tert*-N linkages bring the extended nonplanar π–π stacking configuration of TNB. This delocalizes excess charges throughout the skeleton and suppresses TNB–H_2O interactions, thereby ensuring structural robustness and excellent anti-dissolution to enable a state-of-the-art cycling lifespan of 180 000 cycles for aqueous zinc batteries (Fig. 2e). To our best knowledge, such a top-class cycling lifespan sets a new record for organic cathode materials in aqueous batteries (Fig. 2f and Table S2).[7,16,27,35,40,49,55,60,62,66,68–74] SEM images, FI-IR spectra and UV-vis spectra of the TNB cathode after long-term cycles prove its structure robustness and anti-dissolution in $ZnSO_4$/H_2O

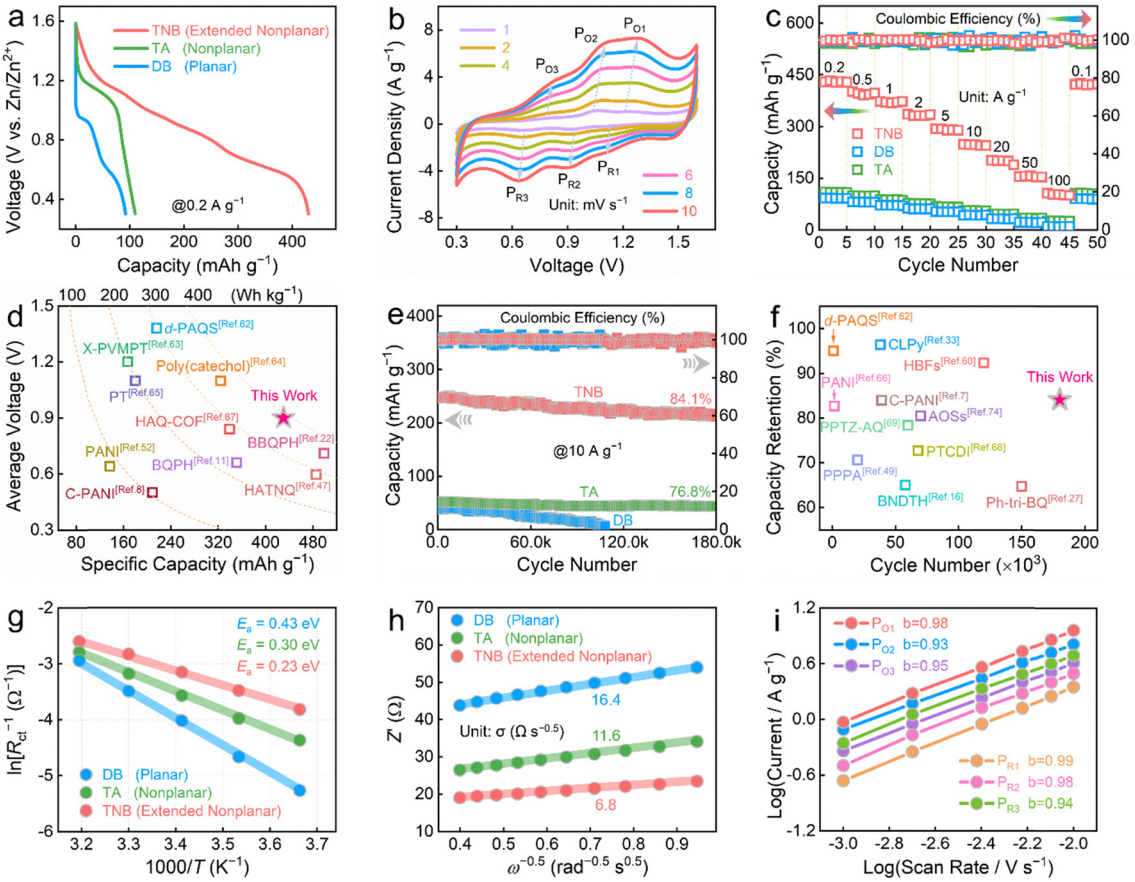

Fig. 2 Electrochemical performance metrics of TNB cathode. (a) GCD curves of TA, DB and TNB cathodes in ZOBs. (b) CV profiles of Zn||TNB cell. (c) Rate capacities. (d) Capacity–voltage contour map of TNB and previously reported organics used in aqueous batteries. (e) Cycling performance. (f) Life comparison of TNB with reported organics used in aqueous batteries. (g) Evaluated E_a values and (h) σ values of ionic carriers of TA, DB and TNB cathodes in ZOBs. (i) Evaluated b values of Zn||TNB battery.

electrolyte (Fig. S17), which is responsible for ultradurable Zn||TNB battery (Fig. S18). Moreover, the battery delivers a highly competitive capacity of 335 mAh g^{-1} (Fig. S19 and Table S3) based on a 12.7 mg $cm^{-2}{}_{TNB}$ cathode, displaying the feasibility of Zn–nitroarene batteries as one of the prospective energy storage solutions.

To date, almost all reported ZOBs with high energy densities are typically estimated based on the active organic materials in the cathode.[12,22,27,47,61] For a more comprehensive comparison, when considering the total mass of the TNB cathode, consumable Zn anode, and $ZnSO_4$ electrolyte, the Zn||TNB battery still delivers an energy density of 160 Wh $kg^{-1}{}_{cell}$ (Fig. S15c), which holds great potential to compete with a recently reported value (105.1 Wh $kg^{-1}{}_{cell}$).[75] The excellent comprehensive electrochemical performances of TNB in terms of rate capacity, energy density and cyclic stability make it a promising cathode material for advanced ZOBs. These results also confirm the high compatibility between the Zn anode and TNB cathode, which points to a new paradigm for developing advanced ZOBs.

To rationalize the significant performance differences between DB, TA and TNB cathodes in ZOBs, we further studied their interfacial redox processes and charge storage kinetics. The activation energy (E_a) of interfacial redox processes of TNB can be revealed *via* fitting electrochemical impedance spectra (EIS, Fig. S20) based on the relationship between charge transfer resistance (R_{ct}) and temperature (T). The E_a value for extended nonplanar TNB is 0.23 eV (Fig. 2g), which is much lower than those of planar DB (0.43 eV) and nonplanar TA (0.30 eV). By circumventing the Coulomb repulsion associated with single-ion hosting in unipolar organics,[76] the co-storage of Zn^{2+} and SO_4^{2-} cation/anion activates proton-like low-activation-energy interfacial redox reactions, affording efficient energy storage in the TNB cathode. It shows that the nonplanar configuration of TNB can activate a fast interfacial redox reaction to fully access redox-active groups in the TNB cathode.

Moreover, the linear relationship between the real part of impedance (Z') of EIS and the reciprocal of the square root of angular frequency ($\omega^{-0.5}$) was fitted to gain the ionic diffusion resistance (σ).[20] Among the three organics, TNB delivers the lowest σ value of 6.8 Ω $s^{-0.5}$ (Fig. 2h), revealing fast ion transport for achieving a high-power Zn||TNB cell. Thanks to the π-conjugated nonplanar steric structure, TNB allows for the full exposure of quadruple nitro sites and dual *tert*-N species, coordinating with Zn^{2+} and SO_4^{2-} with low energy barriers. Based on Dunn's method,[49,70] the six oxidation–reduction peaks of CV profiles (Fig. 2b) display high b values of 0.93–0.99 (Fig. 2i),

signifying the surface-dominant capacitive charge storage of the TNB cathode accompanied by the slight diffusion-limited process (Fig. S21a). Based on the galvanostatic intermittent titration technique (GITT), the TNB cathode achieves a high ion diffusion coefficient (D) with an average value of 10^{-8} $cm^2\,s^{-1}$ (Fig. S21b). These results reveal the high-kinetics and stable energy storage behavior of TNB, which originates from its nonplanar extended conjugation and low-steric-barrier redox-active structure, making for full utilization of ambipolar active motifs and rapid ion migration.

Encouraged by the outstanding electrochemical metrics of the TNB cathode, its charge storage mechanism in ZOBs was analyzed *via* FT-IR spectra and X-ray photoelectron spectroscopy (XPS) characterizations. Seven (dis)charged markers (A, B, C, D, E, F, and G) of the GCD profile of the Zn||TNB cell at 0.2 A g^{-1} were collected to reveal the redox process of TNB (Fig. 3a). In the 2D contour map of FT-IR spectra (Fig. 3b), two characteristic peaks at 1587 and 1352 cm^{-1} (state A) can be ascribed to the stretching vibration of the stretching vibration of the nitro group.[50] The nitro signal remains almost unchanged during discharge (state A → B) and gradually weakens after further discharge proceeding (state B → C → D), implying its n-type reaction activity for the uptake of cationic carriers in the low-potential region. On the contrary, the peak signal of C–N species at 1272 cm^{-1} appears (state A → B),[69] and remains constant during subsequent discharge (state B → C → D), verifying its p-type redox activity for the removal of SO_4^{2-} anions in the high-potential area. In the following recharging process (state D → E → F → G), all adsorption signals exhibit opposite trends due to the release of Zn^{2+} ions from nitro sites and the uptake of SO_4^{2-} anions at *tert*-N centers. Thus, n-type nitro and p-type *tert*-N groups of TNB are identified as ambipolar redox-active motifs to afford reversible (de)coordination reactions with fused anion–cation storage (Fig. 3c).

XPS analysis was performed on Zn 2p and S 2p signals to monitor the changes of Zn^{2+} cations and SO_4^{2-} anions in the TNB cathode during a discharge–charge cycle (Fig. 3d and e). During discharge (state B → C → D), the Zn 2p signal gradually increases due to Zn^{2+} coordination, whereas it decreases during charging (state D → E → F) as Zn^{2+} is removed (Fig. 3d). On the contrary, the S 2p signal exhibits an obvious decrease after discharging (state A → B) and reverts to the initial state in the following recharging process (state F → G, Fig. 3e). These results indicate the reversible (de)coordination of SO_4^{2-} and Zn^{2+} ions. Of note, given the moderately acidic $ZnSO_4/H_2O$ solution (pH ≈ 4.4) and the small-sized solvated H^+ ions, identifying whether H^+ serves as the charge carrier is also essential (Fig. S22). Zn||TNB battery using H_2SO_4/H_2O

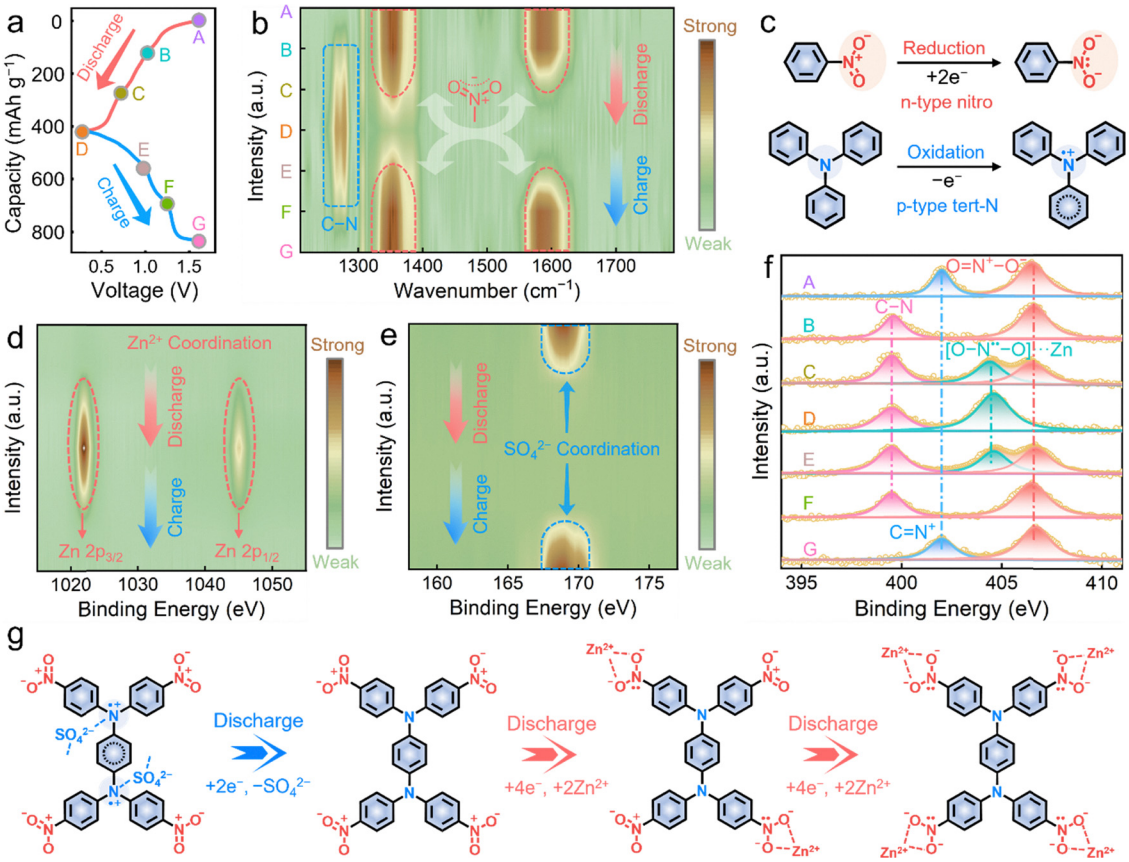

Fig. 3 Structural evolution of TNB cathode during the operation of Zn||TNB battery. (a) A capacity-potential curve. (b) Overview of FT-IR spectra at the marked points in the GCD profile. (c) Redox mechanisms of n-type nitro and p-type *tert*-N groups. *Ex situ* XPS spectra of (d) Zn 2p, (e) S 2p, and (f) N 1s. (g) Anion–cation redox storage mechanism.

electrolyte (pH ≈ 4.4) delivers a low capacity of 8 mAh g^{-1} (Fig. S22a), suggesting the negligible contribution of protons in electrochemical reactions. The lack of flake zinc hydroxide also excludes the participation of protons in the discharged TNB cathode (Fig. S22b). Moreover, there is no UV–Vis absorption signal for a fully reduced TNB cathode in $ZnSO_4/H_2O$ electrolyte (Fig. S22c), indicating its robust structure during the electrochemical reaction process.

Furthermore, high-resolution N 1s XPS spectra were analyzed to further unravel the redox behaviors of the TNB cathode during battery operation (Fig. 3f). A deconvoluted peak at 402.0 eV can be attributed to C═N^+ species formed at state A, confirming the p-type redox activity of C–N groups. During discharge (state A → B), C═N^+ moieties disappear, accompanied by the generation of C–N groups because of the liberation of SO_4^{2-} ions (state B → C → D), proving the redox reactions between C–N sites and SO_4^{2-} anions in the high-potential region. The rearrangement of C–N covalent bonds into C═N^+ species indicates SO_4^{2-}-driven redox reactions (Fig. 3f), rather than physisorption or electrolyte-related artifacts. In contrast, NO_2 motifs at 406.5 eV gradually decrease by taking part in the reduction reaction during the low-potential discharging process (state B → C → D) to form [O–$N^{\bullet\bullet}$–O]···Zn moieties at 404.5 eV. During the recharge process (state D → E → F → G), all signals achieve reversible evolution owing to Zn^{2+} decoordination from n-type nitro motifs and the uptake of SO_4^{2-} anions at p-type *tert*-N sites. Overall, FT-IR spectra (Fig. 3b) and XPS spectra (Fig. 3d–f) confirm the reversible multi-redox utilization of nitro and *tert*-N groups. The structural change of NO_2 and C–N moieties in the TNB cathode agrees with NO_2 groups in the DB cathode and C–N groups in the TA cathode (Fig. S23). It is worth noting that nitroarenes may be converted into amino compounds *via* H^+-coupled irreversible multielectron reduction.[77] Evidently, nitro motifs of the TNB cathode are not converted into amine species in a slightly acidic $ZnSO_4/H_2O$ electrolyte (Fig. S24), thus affording a highly reversible Zn^{2+} (de)coordination process.

Spectral results demonstrate the ambipolar charge storage behavior of TNB with alternating reactions of contrary ionic carriers in multisite motifs, entailing SO_4^{2-}-coupled *tert*-N redox in the high-potential range and Zn^{2+}-coupled nitro redox in the low-voltage domain (also confirmed by GCD results, Fig. S25–S27). The cation/anion co-storage redox mechanism of the TNB cathode can also be observed in aqueous $Zn(OTf)_2$ and $ZnCl_2$ electrolytes, highlighting its broad electrochemical compatibility across different aqueous electrolytes (Fig. S28). The experimental capacity of the TNB cathode is 430 mAh g^{-1} (Fig. 2a), which is close to its theoretical value of 452 mAh g^{-1}, corresponding to a ≈10 e^- redox charge storage process involving four 2 e^- nitro groups and two 1 e^- *tert*-N groups. By harnessing the synergistic merits of planar DB (multielectron nitro redox) and nonplanar TA (low energy barrier and structural insolubility), two rotating *tert*-N linkages afford the extended π-aromatic nonplanar structure of TNB, which thus fully exposes redox-active nitro/*tert*-N motifs to allow for 98.9% utilization with a low activation energy of 0.23 eV (*vs.* 0.43 eV of DB and 0.30 eV of TA, Fig. 2g) *via* co-storing Zn^{2+} and SO_4^{2-} ions (Fig. 3b–f), giving excellent electrochemical activity and stability.

A pouch battery (4 × 4 cm^2) composed of the TNB cathode (12.5 mg cm^{-2}), Zn anode and 3 M $ZnSO_4/H_2O$ electrolyte was further assembled to evaluate its long-term cycling stability. The battery delivers a high capacity of 178 mAh g^{-1} after 3000 cycles at 10 A g^{-1} with 95.2% capacity retention (Fig. S29). Meanwhile, two pouch batteries in series can power a lamp plate (inset of Fig. S29), demonstrating a promising practical prospect. Overall, spectral characterization (Fig. 3a–f and Fig. S23 and S24) and electrochemical analysis (Fig. S22 and S25) reveal that the TNB cathode starts a consecutive three-step 10 e^- ambipolar redox reaction (Fig. 3g). It corresponds to the three pairs of redox peaks observed in CV profiles (Fig. 2b), where the voltage gap (0.40 V) between the anion-active and cation-active plateaus is comparable to previously established bipolar systems (0.30–0.38 V).[32,74] The process involves an initial 2 e^- *tert*-N redox with two SO_4^{2-} anions (P_{O1}/P_{R1}), followed by two consecutive 8 e^- reductions at the two nitro sites in a bipedal-like fashion (*i.e.*, two nitro groups functioning cooperatively as two 'legs'), with each nitro reduction coordinated by two Zn^{2+} ions (P_{O2}/P_{R2} and P_{O3}/P_{R3}). TNB overcomes the barriers of structural instability and high redox energy barriers in every reported organic small molecule, affording excellent performance metrics for state-of-the-art ZOBs (Table S2).

To unravel the electrochemical redox behaviors of TNB, theoretical calculations were further conducted to simulate its molecular structure evolution during battery operation.[78,79] In the optimal TNB structure, Zn^{2+} cation coordinated with two oxygen motifs of the nitro motif and SO_4^{2-} anion bound to the *tert*-N site are thermodynamically the most stable coordination geometries (Fig. S30). According to the minimum energy rule, the optimized anion–cation coordination structures of TNB were imitated, which proves the stable three-step continuous 10 e^- redox reaction pathway. In the charge process (step 1), the binding energy (ΔE) demanded for SO_4^{2-} anions to combine with *tert*-N sites of pristine TNB is −4.12 eV (Fig. 4a and Fig. S31), which forms the anion-doped TNB–SO_4^{2-} complex (state I). In the subsequent discharge process, TNB starts a two-step reduction reaction, in which two Zn^{2+} cations first couple with two diagonal nitro groups (step 2), and then, the other two Zn^{2+} cations coordinate with the residual two nitro motifs (step 3). The ΔE values required for step 2 and step 3 are −13.51 and −5.43 eV, respectively, promoting the formation of cation-coordinated TNB–2Zn^{2+} (state II) and TNB–4Zn^{2+} (state III) products. As a consequence, the favorable anion–cation binding environment promises the rapid and stable multielectron reaction process of the TNB cathode in ZOBs.

The electron structure and molecular conjugation effect of TNB were unraveled by the π-electron localization function (ELF-π) calculation.[55] The interconnected ELF-π isosurfaces in the TNB skeleton show highly nonplanar π-aromaticity and π-electron delocalization along the extended conjugation structure (Fig. 4b). The charge-density difference iso-surface analysis[80] was conducted to deeply untangle the redox natures of the ion-coupled TNB complex (Fig. 4c). The charge accumulation/consumption around *tert*-N/nitro regions and ionic

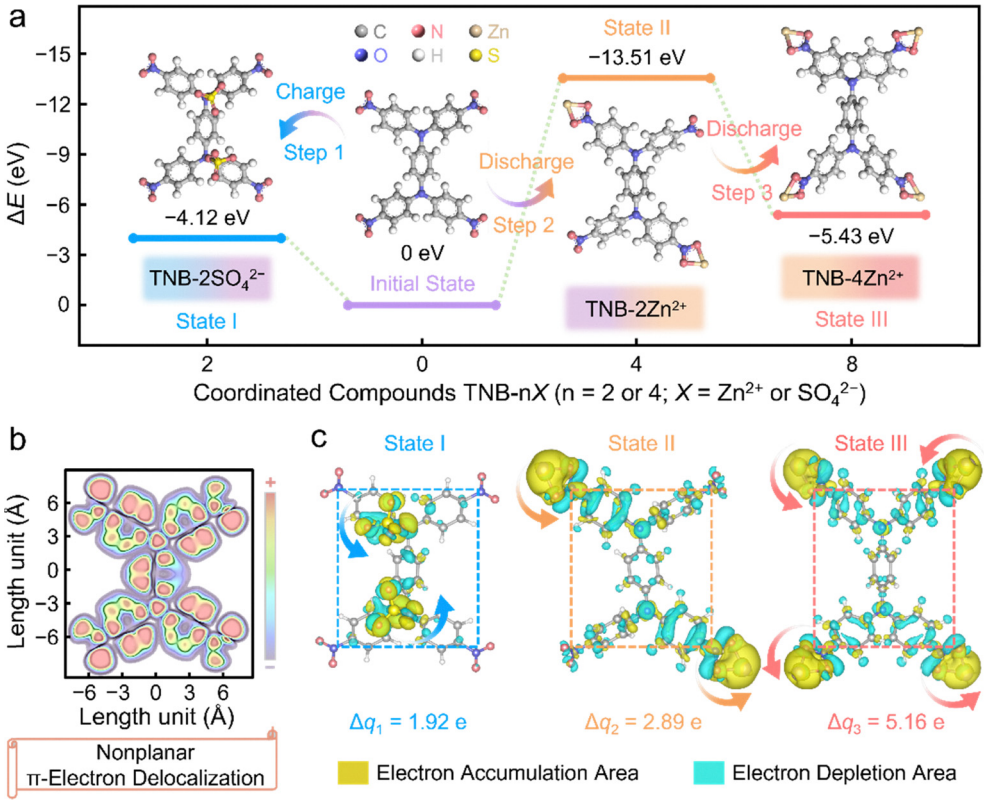

Fig. 4 Theoretical calculation of stepwise 10 e^- anion–cation redox reaction of TNB cathode. (a) Optimized geometries and corresponding ΔE values after the uptake of opposite charge carriers. (b) ELF-π map of TNB. (c) Charge density difference isosurfaces and corresponding Bader charges.

carriers can be monitored, unravelling their strong redox interactions to yield robust geometries. This can also be confirmed by obvious Bader charge transfers of 1.01 e (state I), 3.07 e (state II) and 6.19 e (state III), implying the high redox activity of *tert*-N motifs and nitro moieties. The alternate storage of opposite ions (SO_4^{2-} anions and Zn^{2+} cations) allows the utmost utilization of multi-redox nitro/*tert*-N sites in TNB, giving powerful electrochemical activity and stability.

To demonstrate the electrochemical universality of nonplanar molecular engineering, various multi-redox nonplanar organic small molecules are demonstrated (Fig. 5a–c), including 5,5′-(phenazine-5,10-diyl)diisophthalic acid (PNA), 4,4′,4″,4‴-pyrrolo[3,2-*b*]pyrrole-1,2,4,5(4*H*)-tetrayltetrakis[benzonitrile] (PPT), and *N*1,*N*1,*N*3,*N*3,*N*5,*N*5-hexa(pyridin-4-yl)benzene-1,3,5-triamine (HBT) (Fig. S32). Potential energy curves show that the intramolecular π–π interactions between adjacent aromatic moieties within PNA, PPT, and HBT are stronger than the corresponding H_2O-organic solvation interactions (Fig. 5d–f). Specifically, compared to the repulsive solvation forces caused by H_2O molecules, PNA, HBT, and PPT compounds deliver the most negative *E* values of −21.2, −34.5 and −45.6 kcal mol^{-1} at the stacked layer *R* of 0.31, 0.33, and 0.34 nm, respectively. Such a result indicates strong intramolecular π–π forces of PNA, HBT, and PPT, which are expected to achieve excellent anti-dissolution in aqueous electrolytes.

As a proof of concept, PNA, HBT, and PPT were applied as cathodes to couple with Zn metal anodes for building ZOBs. Impressively, all three ZOBs achieve ultradurable electrochemical activity with an extraordinary lifespan of 180 000 cycles at 10 A g^{-1}, delivering 71.3%/80.6%/85.1% capacity retentions (Fig. 5g–i), respectively. To reveal the potential dissolution behavior of redox species in aqueous electrolytes, three cathodes at different cycles were immersed in aqueous $ZnSO_4$ electrolytes. There is no absorption signal in UV/vis spectra (Fig. S33), confirming the structural stability and anti-dissolution of these nonplanar molecules. These results show the great potential of nonplanar small-molecule cathodes in the development of superstable aqueous ZOBs.

Overall, the demonstrated nonplanar tertiary-N extended molecular structure provides a promising platform for developing insoluble and low-energy-barrier organic small molecules towards better aqueous batteries. Preliminary evidence from carboxylic, cyano, and imine derivatives supports the potential transferability of this design strategy, though further systematic optimization is needed to establish it as a universal principle. Key features include the following: (i) high weight content proportions of redox-active aromatic motifs with strong intramolecular π–π interactions liberate anti-dissolution in aqueous electrolytes; (ii) rotating *tert*-N extended π-conjugated skeletons form nonplanar molecular conformations to efficiently access exposed redox motifs with low energy barriers. More exciting progress can be expected to enrich the organic nonplanar structure library to promote the quest for ever-increasing performances in energy storage communities.

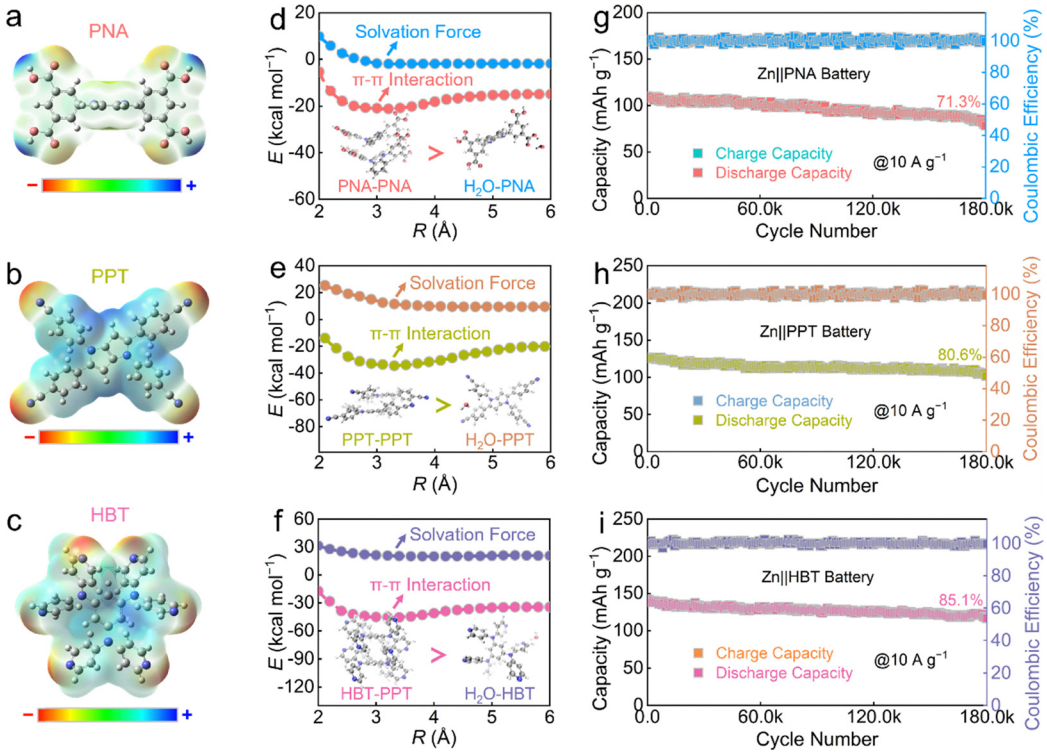

Fig. 5 (a–c) Molecular structures of three types of organic compounds. (d–f) Calculated potential energy curves comparing intramolecular π–π interactions between adjacent aromatic moieties with their respective H_2O-organic solvation interactions for (d) PNA, (e) PPT, and (f) HBT. (g–i) Cycling stability of three organic cathodes in aqueous $ZnSO_4$ electrolyte.

Conclusion

In conclusion, a nonplanar multi-site-redox TNB cathode with dual-electron-donating rotational *tert*-N sites and quadruple two-electron-accepting nitro groups is demonstrated as a new type of cathode material for activating ultrastable ZOBs. We harness the strong intramolecular π–π interactions (exceeding the H_2O dissociation energy in aqueous electrolytes) to inhibit dissolution of the nitroarene cathode. The extended nonplanar conjugated structure of TNB allows full accessibility of low-steric-barrier nitro and *tert*-N redox sites with low energy barriers and, more importantly, promises insolubility in aqueous electrolytes to push the cycle lifespan of ZOBs to a record level. Systemic investigations suggest the 2 e^- *tert*-N redox for SO_4^{2-} anion storage and 8 e^- nitro reactions for Zn^{2+} cation storage in TNB cathode, delivering superior capacity and large-current survivability. Furthermore, the nonplanar structure design is transferable to the development of other insoluble redox-active compounds, as exemplified by carboxylic, cyano, and imine derivatives. These proof-of-concept results suggest that this strategy may inspire further exploration of nonplanar molecular engineering for ZOBs. This study paves a new path to develop various nitroaromatic materials and other potential insoluble low-energy-barrier organic molecules to achieve superstable cycles without sacrificing capacity, which would inspire more related nonplanar structure investigations of high-performance organic materials towards advanced energy storage.

Author contributions

Z. Y. S. conceived the idea, designed the project, and wrote the original paper. M. X. L. supervised the research and revised the paper. Z. Y. S., L. H. G., and Y. K. L. performed the data processing and analysis. Q. H. performed the theoretical simulations. Z. Y. S. and M. X. L. contributed to the manuscript review. All authors engaged in discussions related to the manuscript.

Conflicts of interest

The authors declare no conflict of interest.

Data availability

The data that support the findings of this study are available from the corresponding authors upon reasonable request.

Supplementary information (SI): includes experimental process, calculation methods, supplementary characterizations, electrochemical results, supplementary figures (Fig. S1–S33) and supplementary tables (Tables S1–S3). See DOI: https://doi.org/10.1039/d6ee02250b.

Acknowledgements

This work is financially supported by the National Natural Science Foundation of China (No. 22309134, 22272118, and

22172111), the Shanghai Rising-Star Program (23YF1449200), the Zhejiang Provincial Science and Technology Project (2022C01182), and the Fundamental Research Funds for the Central Universities.

Notes and references

1 C. Li, D.-D. Wang, G. S. H. P. Ho, Z. Zhang, J. Huang, K.-T. Bang, C. Y. Lau, S.-Y. Leu, Y. Wang and Y. Kim, *J. Am. Chem. Soc.*, 2023, **145**, 24603–24614.
2 D. J. Kim, D.-J. Yoo, M. T. Otley, A. Prokofjevs, C. Pezzato, M. Owczarek, S. J. Lee, J. W. Choi and J. F. Stoddart, *Nat. Energy*, 2018, **4**, 51–59.
3 M. Yu, N. Chandrasekhar, R. K. M. Raghupathy, K. H. Ly, H. Zhang, E. Dmitrieva, C. Liang, X. Lu, T. D. Kühne, H. Mirhosseini, I. M. Weidinger and X. Feng, *J. Am. Chem. Soc.*, 2020, **142**, 19570–19578.
4 J. C. Russell, V. A. Posey, J. Gray, R. May, D. A. Reed, H. Zhang, L. E. Marbella, M. L. Steigerwald, Y. Yang, X. Roy, C. Nuckolls and S. R. Peurifoy, *Nat. Mater.*, 2021, **20**, 1136–1141.
5 S. Chang, J. F. F. Gomez, S. Katiyar, G. Morell and X. Wu, *J. Am. Chem. Soc.*, 2023, **145**, 24746–24754.
6 K. W. Nam, H. Kim, Y. Beldjoudi, T.-W. Kwon, D. J. Kim and J. F. Stoddart, *J. Am. Chem. Soc.*, 2020, **142**, 2541–2548.
7 H. Lv, Z. Wei, C. Han, X. Yang, Z. Tang, Y. Zhang, C. Zhi and H. Li, *Nat. Commun.*, 2023, **14**, 3117.
8 S. Zhang, Y.-L. Zhu, S. Ren, C. Li, X.-B. Chen, Z. Li, Y. Han, Z. Shi and S. Feng, *J. Am. Chem. Soc.*, 2023, **145**, 17309–17320.
9 Y. Mu, J. Nyakuchena, Y. Wang, J. R. Wilkes, T. Luo, M. Goldstein, B. Elander, U. Mohanty, J. L. Bao, J. Huang and D. Wang, *Angew. Chem., Int. Ed.*, 2024, **63**, e202409286.
10 J. Yan, B. Wang, Y. Tang, W. Du, M. Ye, Y. Zhang, Z. Wen, X. Liu and C. C. Li, *Angew. Chem., Int. Ed.*, 2024, **63**, e202400121.
11 Z. Tie, Y. Zhang, J. Zhu, S. Bi and Z. Niu, *J. Am. Chem. Soc.*, 2022, **144**, 10301–10308.
12 S. Li, J. Shang, M. Li, M. Xu, F. Zeng, H. Yin, Y. Tang, C. Han and H. M. Cheng, *Adv. Mater.*, 2023, **35**, 2207115.
13 Z. Xu, M. Li, W. Sun, T. Tang, J. Lu and X. Wang, *Adv. Mater.*, 2022, **34**, 2200077.
14 Z. Jin, Q. Cheng, S. T. Bao, R. Zhang, A. M. Evans, F. Ng, Y. Xu, M. L. Steigerwald, A. E. McDermott, Y. Yang and C. Nuckolls, *J. Am. Chem. Soc.*, 2022, **144**, 13973–13980.
15 X. Guo, P. Apostol, X. Zhou, J. Wang, X. Lin, D. Rambabu, M. Du, S. Er and A. Vlad, *Energy Environ. Sci.*, 2024, **17**, 173–182.
16 Q. Q. Sun, T. Sun, J. Y. Du, K. Li, H. M. Xie, G. Huang and X. B. Zhang, *Adv. Mater.*, 2023, **35**, 2301088.
17 J. Chu, Z. Liu, J. Yu, L. Cheng, H. G. Wang, F. Cui and G. Zhu, *Angew. Chem., Int. Ed.*, 2023, **63**, e202314411.
18 J. Wang, P. Poizot, A. E. Lakraychi, X. Liu, L. Sieuw, C. Morari and A. D. Vlad, *Nat. Mater.*, 2023, **20**, 665–673.
19 Y. Chen, H. Dai, K. Fan, G. Zhang, M. Tang, Y. Gao, C. Zhang, L. Guan, M. Mao, H. Liu, T. Zhai and C. Wang, *Angew. Chem., Int. Ed.*, 2023, **62**, e202302539.
20 Z. Song, L. Miao, H. Duan, L. Ruhlmann, Y. Lv, D. Zhu, L. Li, L. Gan and M. Liu, *Angew. Chem., Int. Ed.*, 2022, **61**, e202208821.
21 Y. Zhong, Y. Li, J. Meng, X. Lin, Z. Huang, Y. Shen and Y. Huang, *Energy Storage Mater.*, 2021, **43**, 492–498.
22 W. Li, H. Xu, H. Zhang, F. Wei, L. Huang, S. Ke, J. Fu, C. Jing, J. Cheng and S. Liu, *Nat. Commun.*, 2023, **14**, 5235.
23 L. Lin, Z. Lin, J. Zhu, K. Wang, W. Wu, T. Qiu and X. Sun, *Energy Environ. Sci.*, 2023, **16**, 89–96.
24 Z. Tian, V. S. Kale, Y. Wang, S. Kandambeth, J. Czaban-Jóźwiak, O. Shekhah, M. Eddaoudi and H. N. Alshareef, *J. Am. Chem. Soc.*, 2021, **143**, 19178–19186.
25 Q.-Q. Sun, J.-Y. Du, T. Sun, Z.-B. Zhuang, Z.-L. Xie, H.-M. Xie, G. Huang and X.-B. Zhang, *Adv. Mater.*, 2024, **36**, 2313388.
26 X. Huang, X. Qiu, W. Wang, J. Li, Z. Li, X. Yu, J. Ma and Y. Wang, *J. Am. Chem. Soc.*, 2023, **145**, 25604–25613.
27 L. Lin, Z. Xue, T. Qiu, J. Zhu, G. Zhang, H. Zhan, K. Wang and X. Sun, *Energy Environ. Sci.*, 2024, **17**, 6499–6506.
28 J. Zhu, Z. Tie, S. Bi and Z. Niu, *Angew. Chem., Int. Ed.*, 2024, **63**, e202403712.
29 S. Zheng, D. Shi, D. Yan, Q. Wang, T. Sun, T. Ma, L. Li, D. He, Z. Tao and J. Chen, *Angew. Chem., Int. Ed.*, 2022, **61**, e202117511.
30 Z. Li, J. Tan, Y. Wang, C. Gao, Y. Wang, M. Ye and J. Shen, *Energy Environ. Sci.*, 2023, **16**, 2398–2431.
31 H. Peng, S. Huang, V. Montes-García, D. Pakulski, H. Guo, F. Richard, X. Zhuang, P. Samorì and A. Ciesielski, *Angew. Chem., Int. Ed.*, 2023, **62**, e202216136.
32 N. Wang, Z. Guo, Z. Ni, J. Xu, X. Qiu, J. Ma, P. Wei and Y. Wang, *Angew. Chem., Int. Ed.*, 2021, **60**, 20826–20832.
33 C. Zhang, W. Ma, C. Han, L.-W. Luo, A. Daniyar, S. Xiang, X. Wu, X. Ji and J.-X. Jiang, *Energy Environ. Sci.*, 2021, **14**, 462–472.
34 P. Yi, Z. Li, L. Ma, B. Feng, Z. Liu, Y. Liu, W. Lu, S. Cao, H. Fang, M. Ye and J. Shen, *Adv. Mater.*, 2024, **36**, 2414379.
35 Y. Liu, Y. Lu, A. Hossain Khan, G. Wang, Y. Wang, A. Morag, Z. Wang, G. Chen, S. Huang, N. Chandrasekhar, D. Sabaghi, D. Li, P. Zhang, D. Ma, E. Brunner, M. Yu and X. Feng, *Angew. Chem., Int. Ed.*, 2023, **62**, e202306091.
36 S. M. Pallasch, M. Bhosale, G. J. Smales, C. Schmidt, S. Riedel, Z. Zhao-Karger, B. Esser and O. Dumele, *J. Am. Chem. Soc.*, 2024, **146**, 17318–17324.
37 L. Yan, Q. Zhu, Y. Qi, J. Xu, Y. Peng, J. Shu, J. Ma and Y. Wang, *Angew. Chem., Int. Ed.*, 2022, **61**, e202211107.
38 U. Mittal, F. Colasuonno, A. Rawal, M. Lessio and D. Kundu, *Energy Storage Mater.*, 2022, **46**, 129–137.
39 Y. Zhao, Y. Huang, F. Wu, R. Chen and L. Li, *Adv. Mater.*, 2021, **33**, 2106469.
40 I. Obraztsov, R. Langer, J. G. A. Ruthes, V. Presser, M. Otyepka, R. Zbořil and A. Bakandritsos, *Energy Environ. Sci.*, 2024, **17**, 8874–8884.
41 J. Kim, Y. Kim, J. Yoo, G. Kwon, Y. Ko and K. Kang, *Nat. Rev. Mater.*, 2022, **8**, 54–70.

42 T. Chen, H. Banda, L. Yang, J. Li, Y. Zhang, R. Parenti and M. Dincă, *Joule*, 2023, **7**, 986–1002.
43 S. Meng, T. He, L. Chen, K. Liao, H. Lu, T. Liu, R. Meng, J. Ma, C. Zhang and J. Yang, *Energy Environ. Sci.*, 2024, **17**, 5162–5172.
44 D. Du, J. Zhou, Z. Yin, G. Feng, W. Ji, H. Huang and S. Pang, *Adv. Energy Mater.*, 2024, **14**, 2400580.
45 W. Li, H. Ma, W. Tang, K. Fan, S. Jia, J. Gao, M. Wang, Y. Wang, B. Cao and C. Fan, *Nat. Commun.*, 2024, **15**, 9533.
46 Y. Zhang, Q. Huang, P. Liu, Y. Lv, Z. Song, L. Gan and M. Liu, *Nat. Commun.*, 2026, **17**, 4001.
47 Y. Chen, J. Li, Q. Zhu, K. Fan, Y. Cao, G. Zhang, C. Zhang, Y. Gao, J. Zou, T. Zhai and C. Wang, *Angew. Chem., Int. Ed.*, 2022, **61**, e202116289.
48 S. Gaber, A. K. Mohammed, B. H. Javaregowda, J. I. Martínez, P. P. Sánchez, F. Gándara, K. Krishnamoorthy and D. Shetty, *Angew. Chem., Int. Ed.*, 2024, **63**, e202409256.
49 F. Ye, Q. Liu, H. Dong, K. Guan, Z. Chen, N. Ju and L. Hu, *Angew. Chem., Int. Ed.*, 2022, **61**, e202214244.
50 X. Liu and Z. Ye, *Adv. Energy Mater.*, 2020, **11**, 2003281.
51 K. Amin, B. C. Baker, L. Pan, W. Mehmood, Z. Hao, R. Nawaz, Z. Wei and C. F. J. Faul, *Adv. Mater.*, 2024, **37**, 2410262.
52 L. Zhong, C. Liu, Y. Zhang, J. Li, F. Yang, Z. Zhang and D. Yu, *Angew. Chem., Int. Ed.*, 2025, **64**, e202413971.
53 J. Wang, X. Guo, P. Apostol, X. Liu, K. Robeyns, L. Gence, C. Morari, J.-F. Gohy and A. Vlad, *Energy Environ. Sci.*, 2022, **15**, 3923–3932.
54 Z. Song, L. Miao, Y. Lv, L. Gan and M. Liu, *Angew. Chem., Int. Ed.*, 2023, **62**, e202309446.
55 T. Sun, W. Zhang, Z. Zha, M. Cheng, D. Li and Z. Tao, *Energy Storage Mater.*, 2023, **59**, 102778.
56 Y. Chen, D. Zhang, Y. Qin, C. Hu, L. Miao, Y. Lv, Z. Song, L. Gan and M. Liu, *Nat. Commun.*, 2026, **17**, 3599.
57 X. Shi, A. Yi, Q. Liu, Y. Zhang, S. Lin and X. Lu, *ACS Nano*, 2023, **17**, 25005–25013.
58 Y. Xiu, A. Mauri, S. Dinda, Y. Pramudya, Z. Ding, T. Diemant, A. Sarkar, L. Wang, Z. Li, W. Wenzel, M. Fichtner and Z. Zhao-Karger, *Angew. Chem., Int. Ed.*, 2022, **62**, e202212339.
59 H. Cui, D. Zhang, Z. Wu, J. Zhu, P. Li, C. Li, Y. Hou, R. Zhang, X. Wang, X. Jin, S. Bai and C. Zhi, *Energy Environ. Sci.*, 2024, **17**, 114–122.
60 W. Du, Y. Zhang, H. Duan, Y. Lv, Z. Song, L. Gan and M. Liu, *Sci. Adv.*, 2026, **12**, eaec9924.
61 W. Sun, F. Zhu, W. Guo and Y. Fu, *J. Am. Chem. Soc.*, 2025, **147**, 5089–5098.
62 X. Ren, D. Tao, S. Cui, T. Li, Y. Cao and F. Xu, *Energy Storage Mater.*, 2023, **63**, 102992.
63 G. Studer, A. Schmidt, J. Büttner, M. Schmidt, A. Fischer, I. Krossing and B. Esser, *Energy Environ. Sci.*, 2023, **16**, 3760–3769.
64 N. Patil, C. de la Cruz, D. Ciurduc, A. Mavrandonakis, J. Palma and R. Marcilla, *Adv. Energy Mater.*, 2021, **11**, 2100939.
65 C. Han, H. Li, Y. Li, J. Zhu and C. Zhi, *Nat. Commun.*, 2021, **12**, 2400.
66 L. Zhong, C. Liu, Y. Zhang, J. Li, F. Yang, Z. Zhang and D. Yu, *Joule*, 2023, **7**, 971–985.
67 W. Wang, V. S. Kale, Z. Cao, Y. Lei, S. Kandambeth, G. Zou, Y. Zhu, E. Abouhamad, O. Shekhah, L. Cavallo, M. Eddaoudi and H. N. Alshareef, *Adv. Mater.*, 2021, **33**, 2103617.
68 F. Qiao, J. Wang, R. Yu, M. Huang, L. Zhang, W. Yang, H. Wang, J. Wu, L. Zhang, Y. Jiang and Q. An, *ACS Nano*, 2023, **17**, 23046–23056.
69 L. W. Luo, C. Zhang, W. Ma, C. Han, X. Ai, Y. Chen, Y. Xu, X. Ji and J. X. Jiang, *Adv. Mater.*, 2024, **36**, 2406106.
70 L. Xie, K. Xu, W. Sun, Y. Fan, J. Zhang, Y. Zhang, H. Zhang, J. Chen, Y. Shen, F. Fu, H. Kong, G. Wu, J. Wu, L. Chen and H. Chen, *Angew. Chem., Int. Ed.*, 2023, **62**, e202300372.
71 Y. Lin, H. Cui, C. Liu, R. Li, S. Wang, G. Qu, Z. Wei, Y. Yang, Y. Wang, Z. Tang, H. Li, H. Zhang, C. Zhi and H. Lv, *Angew. Chem., Int. Ed.*, 2023, **62**, e202218745.
72 C. Wang, R. Li, Y. Zhu, Y. Wang, Y. Lin, L. Zhong, H. Chen, Z. Tang, H. Li, F. Liu, C. Zhi and H. Lv, *Adv. Energy Mater.*, 2023, **14**, 2302495.
73 X. Peng, Y. Xie, A. Baktash, J. Tang, T. Lin, X. Huang, Y. Hu, Z. Jia, D. J. Searles, Y. Yamauchi, L. Wang and B. Luo, *Angew. Chem., Int. Ed.*, 2022, **61**, e202203646.
74 Z. Song, Q. Huang, Y. Lv, L. Gan and M. Liu, *Angew. Chem., Int. Ed.*, 2025, **64**, e202418237.
75 Y. Zhang, M. Li, Z. Li, Y. Lu, H. Li, J. Liang, X. Hu, L. Zhang, K. Ding, Q. Xu, H. Liu and Y. Wang, *Angew. Chem., Int. Ed.*, 2025, **64**, e202410342.
76 W. Sun, C. Zhou, Y. Fan, Y. He, H. Zhang, Z. Quan, H. Kong, F. Fu, J. Qin, Y. Shen and H. Chen, *Angew. Chem., Int. Ed.*, 2023, **62**, e202300158.
77 Z. Chen, H. Su, P. Sun, P. Bai, J. Yang, M. Li, Y. Deng, Y. Liu, Y. Geng and Y. Xu, *Proc. Natl. Acad. Sci. U. S. A.*, 2022, **169**, e2116775119.
78 N. Wang, R. Zhou, H. Li, Z. Zheng, W. Song, T. Xin, M. Hu and J. Liu, *ACS Energy Lett.*, 2021, **6**, 1141–1147.
79 J. Yang, H. Hua, H. Yang, P. Lai, M. Zhang, Z. Lv, Z. Wen, C. C. Li, J. Zhao and Y. Yang, *Adv. Energy Mater.*, 2023, **13**, 2204005.
80 H. Lu, J. Hu, K. Zhang, Y. Zhang, B. Jiang, M. Zhang, S. Deng, J. Zhao, H. Pang and B. Xu, *Adv. Mater.*, 2024, **36**, 2408396.